Int. J. Appl. Ceram. Technol., 8 [1] 214–226 (2011)
DOI:10.1111/j.1744-7402.2009.02431.x

International Journal of
Applied Ceramic TECHNOLOGY
Ceramic Product Development and Commercialization

Anisotropy of the Mechanical and Thermoelectric Properties of Hot-Pressed Single-Layer and Multilayer Thick $Ca_3Co_4O_9$ Ceramics

Driss Kenfaui,* Daniel Chateigner, Moussa Gomina, and Jacques Guillaume Noudem

CRISMAT, UMR 6508 CNRS/ENSICAEN, Université de Caen Basse-Normandie, 14050 Caen Cedex 04, France

$Ca_3Co_4O_9$ (349) thermoelectric (TE) ceramics were prepared by hot-pressing (HP) process under various stress levels up to 30 MPa. Microstructure investigations have revealed strong enhancements of the bulk density and the texture strength, and a remarkable decrease of the in-plane grain boundary density as the HP stress, σ, is increased. The mechanical properties obtained from nanoindentation and three-point bending tests, and the TE properties were correlated to the microstructure. The influence of the HP stress level on these properties was examined in the parallel (*c*) and perpendicular (*ab*) directions to the pressing axis. Hardness (H^{ab} and H^{c}) and elastic modulus (E^{ab} and E^{c}) values were shown to increase remarkably with the HP stress level and the anisotropy ratio between out-of-plane and in-plane resistivity values $\left(\frac{\rho^c}{\rho^{ab}}\right)$ too. As ρ^{ab} was considerably reduced and the Seebeck coefficient, S^{ab}, remains constant when σ is raised, the power factor, PF^{ab}, was greatly improved for the higher stress values. $\left(\frac{\rho^c}{\rho^{ab}}\right)_{300\,K}$ and $PF^{ab}{}_{900\,K}$ are 64 and 595 $\mu W.m^{-1}.K^{-2}$, respectively, for the HP samples processed under 30 MPa. Thick specimens usable in practical devices were obtained by HP stacked single layers. Their microstructure was investigated and correlated to the TE and mechanical properties.

Introduction

Thermoelectric (TE) materials have received increasing attention because of their potential applications in the fields of energy conversion: the Seebeck effect allows electricity generation from dissipated heat while

*driss.kenfaui@ensicaen.fr

the Peltier effect can be used for cooling by pumping heat. Layered cobalt oxides $Ca_3Co_4O_9$ (349), reported[1–3] to possess a large thermopower coexisting with low electrical resistivity, are among the potential candidates for these applications. Furthermore, 349 oxides resist oxidation in air at high temperature, exhibit high chemical and thermal stabilities, and do not contain toxic elements, in contrast to other oxides like $NaCo_2O_4$, Bi–Ca/Sr–Co–O, and Bi–Pb–Sr–Co–O.[4–8] All these compounds exhibit a large conversion efficiency characterized by the figure-of-merit $ZT = \frac{S^2 \times T}{\rho \times \kappa}$ (S is the Seebeck coefficient, T the absolute temperature, ρ the electrical resistivity, and κ the thermal conductivity). The discovery of these performances has thrown attention on the need for 349 polycrystalline bulk and has boosted the exploration of various processing methods with the aim to increase the properties via fully mastered microstructures. Spark plasma sintering (SPS), magnetic alignment (MA), and hot-pressing (HP) processes[7,9,10] have been reported to allow elaboration of 349 ceramics with high texture and/or strong bulk density, which both improve significantly the TE performances of 349 oxides.

Up to now, these materials have not been integrated in application devices when elaborated by HP process, due to their low thickness and the lack of data in the literature on their thermomechanical behavior.

In this work, we report on the 349 TE ceramics prepared by HP under different stress levels up to 30 MPa. The microstructure and texture features of the samples are investigated and correlated to the elaboration parameters, and are shown to govern the mechanical and TE properties.

Thick samples were prepared by HP a stack of single-layer samples primarily elaborated under 30 MPa. The microstructure, mechanical, and TE properties of these multilayer samples are also investigated and compared with those of the single-layer samples.

Experiment Procedure

Sintering Conditions

Polycrystalline 349 ceramics were prepared by conventional solid-state synthesis technique from $CaCO_3$ and Co_3O_4 powders. These starting precursors were thoroughly mixed in stoichiometric ratios for 30 min in dry condition. The mixture was firstly heated at 900°C for 24 h in air to assure the carbonates decomposition, then finely ground and uniaxially cold-pressed at 92 MPa into 4.2-mm-thick pellets with a diameter of 25 mm. One of the pellets was sintered at 920°C for 24 h with no applied stress (reference sample). The others pellets were set in the furnace between two silver sheets (0.125 mm thick) to avoid any chemical reaction with the alumina-bearing plates at high temperature. The dwell temperature is chosen 6°C lower than the decomposition temperature[11] of the 349 phase, which is 926°C. The uniaxial stress was applied once the dwell temperature is reached, maintained for 24 h, and then removed before cooling in order to avoid microcracking of the samples. Different HP stress levels were applied: 5, 13, 20, and 30 MPa (HP samples), using a homemade HP device described in more details elsewhere.[12] The resulting thickness of the 349 disks monotonously decreases as the applied stress σ is increased (Table I). Applied stresses beyond 30 MPa lead to samples that may be too thin for use later for different manipulations. All the HP pellets were cut to eliminate the less densified zones, and the parallelepiped samples obtained were polished on their two faces. Five single-layer samples hot-pressed at 30 MPa were stacked and hot-pressed at 920°C and only 10 MPa for 5 h (Fig. 1). The thickness of the resulting 349 multilayer sample is about 2.3 mm.

Microstructure Analysis

The microstructure of 349 ceramics was examined using a Supra 55 scanning electron microscope (SEM, Zeiss, Oberkochen, Germany). The phase purity and the texture of the samples were investigated using X-ray diffraction on a four-circle diffractometer setup equipped with the monochromatized Cu$K\alpha$ radiation and a curved position sensitive detector (CPS 120, INEL, Artenay, France), described in details elsewhere,[13] and within the combined analysis formalism[14] implemented in MAUD.[15] Briefly, this methodology allows the quantitative texture determination of the samples, using a cyclic Rietveld refinement of a series of X-ray diagrams measured at different sample orientations. Because of the expected texture strength in such materials and the axially symmetric texture (induced by the orthotropic deformation under uniaxial pressure), we measured 13 diagrams every 5° in tilt angle χ, for an incident angle of the X-ray beam on the sample of $\omega = 20°$. The instrument contributions (χ and ω broadenings, peak shapes, zero-shifts) were calibrated using the LaB_6 powder standard from NIST. A counting time

Table I. Electrical, Mechanical, and Microstructural–Textural Characteristics of the Hot-Pressed Single-Layer Samples at Various Applied Stresses

Stress, σ (MPa)	0	5	13	20	30
Sample thickness, e (mm)	4.45	$2.2 \leq e \leq 2.5$	$1.2 \leq e \leq 1.5$	$0.6 \leq e \leq 0.9$	$0.4 \leq e \leq 0.6$
Density (% theoretical)	60	90.5	94.8	95.1	96
In-plane grain size (μm)	≤ 5	≤ 9	≤ 12	≤ 14.5	≤ 17
Grain thickness (μm)	≤ 5	—	≤ 0.18	—	≤ 0.12
Max of the {001} poles (mrd)	3.48	7.82	9.28	15.36	22.15
Cell parameters after refinement					
a (Å)	4.8427(6)	4.839(1)	4.8911(5)	4.884(5)	4.8573(3)
b (Å)	36.561(3)	36.32(1)	36.339(5)	36.330(4)	36.526(3)
c (Å)	10.8390(7)	10.8197(4)	10.8227(2)	10.8190(2)	10.8547(3)
β (°)	97.96(1)	97.833(5)	97.806(2)	97.766(2)	97.913(3)
Reliability factors (Rietveld)					
R_w (%)	6.81	5.52	3.33	3.60	3.26
R_{Bragg} (%)	5.32	3.12	2.46	2.62	2.27
$R_{expected}$ (%)	5.89	1.56	1.56	1.54	0.85
Reliability factors (OD)					
R_w (%)	5.01	6.89	3.11	4.26	1.29
R_{Bragg} (%)	4.27	5.30	3.49	4.80	2.67
Mechanical properties					
H_{ab} (GPa)	0.11 ± 0.03	1.5 ± 0.43	2.01 ± 0.27	1.95 ± 0.28	2.08 ± 0.36
H_c (GPa)	—	1 ± 0.15	2.16 ± 0.23	2 ± 0.15	2.31 ± 0.22
$\frac{H^c}{H^{ab}}$	—	0.67	1.07	1.03	1.11
σ_R^{ab} (MPa)	18.4 ± 0.2	197.82 ± 3.96	—	—	249.5 ± 3.5
E_{ab} (GPa)	10.46 ± 1.71	52.79 ± 3.2	52.32 ± 3.33	53.35 ± 4.45	55.8 ± 3.67
E_c (GPa)	—	53.06 ± 2.58	76.88 ± 4.02	73.98 ± 3.07	85.21 ± 5.41
$\frac{E^c}{E^{ab}}$	—	1.01	1.47	1.39	1.53
Thermoelectric properties					
$\rho_{300\,K}^{ab}$ (mΩ cm)	38.81	8.72	6.5	5.88	6.1
$\rho_{300\,K}^{c}$ (mΩ cm)	—	20.83	44.02	189.16	390.13
$\frac{\rho^c}{\rho^{ab}}$	—	2.39	6.77	32.16	63.95
$\rho_{900\,K}^{ab}$ (mΩ cm)	44.1 at 834 K	7.31	—	5.88	5.25
S_{900K}^{ab} (μV/K)	174 at 834 K	169	—	172	174
PF_{900K}^{ab} (μW/m/K^2)	68.8 at 834 K	390	—	501	595.42

of 10 min for each sample orientation was used, and our optical setup provides with a 0.1° peak widths in 2θ. Pole figures obtained here are normalized into multiples of a random distribution (mrd), a unit that does not depend on other factors than orientation. In such units, a sample without preferred orientations exhibits uniform pole figures with 1 mrd levels, while a textured sample shows pole figures with maxima and minima of orientation densities ranging from 0 mrd (absence of crystals oriented in this direction) to infinity (for a single crystal on few directions). The overall texture strength is evaluated through the texture index,[16] which is expressed in mrd^2 units and varies from 1 (random powder) to infinity (perfect texture or single crystal) and is

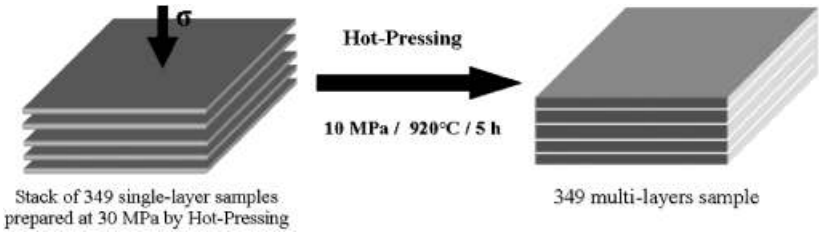

Fig. 1. Hot-pressing stacking process used to elaborate thick samples from the hot-pressing single-layer samples.

used to compare the texture strength of different samples exhibiting similar orientation distributions (ODs). Such normalized pole figures are calculated from the OD of crystallites, refined using the E-WIMV formalism[17] after extraction of the peak intensities during the Rietveld cycles. The OD and profile refinement reliabilities are estimated using conventional reliability factors.[18] During these refinements we used the supercell definition of 349 as described previously.[19]

Mechanical Tests and Thermal Analysis

Instrumented nanoindentation tests were performed on the samples using a XP Nano Indenter® (MTS Systems Eden Prairie, MN) equipped with a Berkovich tip with radius ≤ 20 nm. For each test, impressions were introduced on the mirror-polished sections with 100 μm spacing between them to minimize the possible interaction between the deformed areas. After the indentation load was removed, the load–displacement (–penetration depth) data were used to calculate hardness, H, and elastic modulus (Young's modulus), E. The hardness for an indentation depth, h, can be calculated from the following equation:

$$H = \frac{P_{\max}}{A}$$

where $P_{\max}$ refers to the load measured at the maximum penetration depth, $h_{\max}$, while A refers to the projected contact area between the indenter and the specimen at $P_{\max}$.

The elastic modulus of the specimen, E, is determined from the reduced modulus, E_r, given by

$$E_r = \frac{\sqrt{\pi} \times S}{2 \times \beta \times \sqrt{A}}$$

where $S = \frac{dP}{dh}$ is the elastic stiffness of the specimen–indenter contact, defined as the slope of the initial unloading curve in the load–displacement plot.[20] β is a constant that depends only on the used indenter (more or less symmetrical), and $\beta = 1.0615$ for a Berkovich tip.[21] The modulus, E, can then be calculated as follows:

$$E = \frac{(1 - \nu^2)}{\frac{1}{E_r} - \frac{(1-\nu_i^2)}{E_i}}$$

where ν and ν_i are the Poisson's ratios of the specimen and indenter, respectively, while E_i is the elastic modulus of the indenter.

The strength for our 349 ceramics was determined at room temperature using three-point bending tests. The tested bars were cut from the different samples with almost the same thickness (~ 2 mm) and width (~ 3 mm) to allow a comparison between strength values. We tested bars taken from the reference sample (0 MPa), the HP sample prepared at 5 MPa, and the thick multilayer sample.

The thermal expansion measurements were also performed in the temperature range 50–900°C for the reference and multilayer samples.

Electrical Measurements

The temperature dependence of electrical resistivity was measured perpendicular, ρ^{ab}, and parallel, ρ^{c}, to the HP axis. In the temperature range from 5 to 350 K, the resistivities were measured by the standard DC four-probe method by using a Quantum Design Physical Property Measurement System (Oxford Instruments, Buckinghamshire, U.K.). These measurements were carried out on ~ 4 mm $\times$ 4 mm bar-shaped samples cut from the reference sample, the HP samples, and the multilayer sample using a diamond saw. The resistivity, ρ^{c}, was also studied using the Montgomery method.[22] The high-temperature (from 350 to 900 K) electrical resistivity, ρ^{ab}, and Seebeck coefficient, S^{ab}, were simultaneously measured in a direction perpendicular to the

pressing axis using a ZEM-3 apparatus (ULVAC-RIKO, Yokohama, Japan).

Results and Discussion

Microstructural and Textural Studies

Figure 2 shows SEM micrographs of fractured surfaces of the reference (0 MPa), HP, and multilayer samples performed on the planes containing the pressing axis (indicated by an arrow on inset of Figs. 2a and b). As shown in Fig. 2a, the microstructure of the reference sample exhibits small grains with typical sizes $< 5\,\mu m$, which appear to be loosely assembled and randomly oriented. A large number of pores are also observed that greatly reduce the bulk density and deteriorate the electrical and mechanical properties. In the HP sample processed at 13 MPa (inset of Fig. 2a), the grains are transformed into platelets under the HP effect and their in-plane size increases from 5 to about 9 μm, while their thickness decreases drastically to values smaller than 0.18 μm. Much of the porosity is removed for this applied stress level, which improves the relative bulk density considerably from 60% to 94.6% of the theoretical density. We also observe large zones with an alignment of platelets stacked up along the HP axis. For the sample hot-forged at 30 MPa (Fig. 2b), the platelets are much more extended and their in-plane size reaches 17 μm, which reduces significantly the grain boundary density in the plane perpendicular to the pressing axis. Consequently, the thickness of the platelets is reduced to values below 0.12 μm, which increases the grain boundary density in the direction parallel to the pressing axis. The relative bulk density is strengthened (96%) and the connection between the platelets improved. Figure 2b also shows stronger full alignment of the platelets that are homogenously distributed and compactly stacked up along the pressing axis.

From these observations, we can deduce that when the pressing stress is raised, the 349 ceramics bulk density, the alignment of platelets, and the out-of-plane grain boundary density increase drastically, while the in-plane grain boundary density decreases significantly.

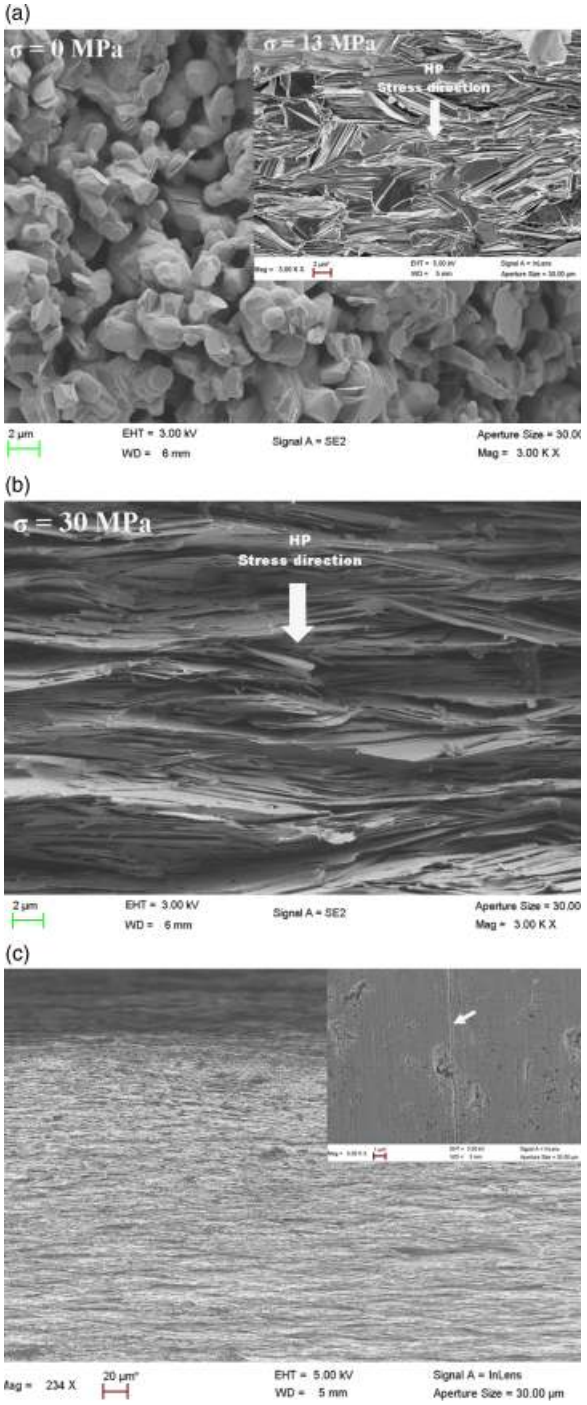

Fig. 2. Scanning electron micrographs of fractured surfaces of the $Ca_3Co_4O_9$ ceramics: (a) reference sample processed without any applied stress σ. Inset shows the hot-pressing sample at 13 MPa. (b) Hot-pressing sample at 30 MPa. (c) Multilayer sample prepared by the hot-pressing stacking process. Inset shows the interface between the initial single-layer samples processed at 30 MPa observed on the mirror-polished cross section of the multilayer sample.

Figure 2c shows a cross-sectional view of the multilayer sample. It appears that the internal alignment of the platelets in the initial single-layer samples used for the stack elaboration is not perturbed by the HP. The multilayer sample morphology shows a densified 349 ceramic with platelets strongly oriented in the whole thickness. We could not distinguish any interface between the primary single-layer samples at such a low magnification. A thin interface with a mean width that does not exceed 50 nm was observed at much higher magnifications on a mirror-polished cross section (arrow in the inset of Fig. 2c), which should not cause a noticeable perturbation on the microstructure or on the homogeneity of the physical properties throughout the thickness of the whole stack. The interface width could be reduced by increasing the stress and/or the dwell time applied during the HP of the stack. Thus, the interface quality could be improved. This shows that thick viable samples of any desired thickness can be tailored by the stacking of elementary layers.

The combined analysis of the HP single layer processed at 30 MPa (Fig. 3a) shows a strong decrease of the 00l lines of the 349 structure with the tilt angle χ, as an indication of a strong texture. After refinement, the calculated diagrams compare well with the experiments (Fig. 3b), within reliability factors as low as $R_w = 3.26\%$, $R_{Bragg} = 2.27\%$, $R_{expected} = 0.85\%$, giving a goodness of fit (GoF) of 14.7 (Table I). The resulting cell parameters after refinement are $a = 4.8573(3)$ Å, $b = 36.526(3)$ Å, $c = 10.8547(3)$ Å, $\beta = 97.913(3)$ (Table I), coherent with the usual bulk values of this phase, and a mean isotropic crystallite size of 654(45) nm, in accordance with the mean dimension of the grains as revealed by SEM examination. This latter point testifies for the HP process to afford strongly oriented grains.

The combined OD refinement allows the reconstruction of the {020}, {001}, and {100} pole figures (Fig. 4a). This refinement was obtained with reliability factors of the OD of $R_w = 1.29\%$ and $R_{Bragg} = 2.67\%$ (Table I), which are very low values for such a high texture strength of $F^2 = 6\ \text{mrd}^2$. The pole figures clearly show that the $\langle 001 \rangle^*$ directions (normal to the {001} planes) are strongly aligned parallel to the stress axis (center of the pole figures), with a maximum of the {001} poles of around 22 mrd, the largest value obtained to date on 349 ceramics. The maximum value of the OD is 118 mrd, and its minimum is 0, indicating that all the crystallites are oriented within the fiber orientation components. The inverse pole figure calculated

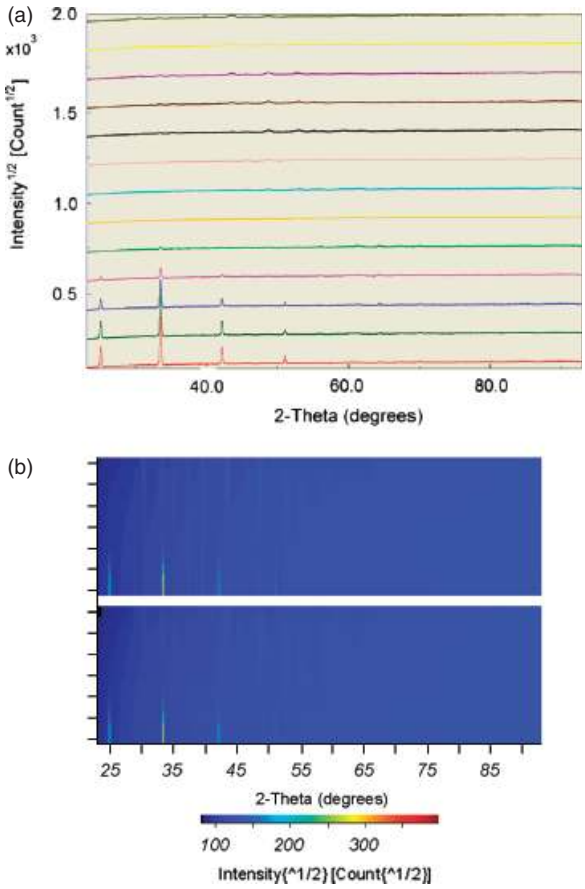

Fig. 3. X-ray diagrams of the single-layer sample prepared at 30 MPa: (a) χ-evolution of the diffracted diagrams. χ goes from 0° (bottom diagram) to 60° (top diagram) by steps of 5°, and (b) experimental (bottom) and refined (top) series of diagrams.

for the pressing axis indicates that no other significant orientation component than the $\langle 001 \rangle$ fiber exists (Fig. 4b) and corresponds to levels of orientations along the pressure axis up to 57 mrd.

The quantitative texture analysis of the HP sample processed at 13 MPa indicates lower crystallographic texture strength. This is shown also in the {020}, {001}, and {100} pole figures (Fig. 5a) culminating at a lower orientation density value of 9.28 mrd at the center of {001}. The Rietveld refinement was obtained with similar reliability factors ($R_w = 3.33\%$, $R_{Bragg} = 2.46\%$, $R_{expected} = 1.56\%$, GoF = 4.5) and cell parameters ($a = 4.8911(5)$ Å, $b = 36.339(5)$ Å, $c = 10.8227(2)$ Å, $\beta = 98.806(2)$), and the OD refinement was also satisfactory ($R_w = 3.11\%$ and $R_{Bragg} = 3.49\%$).

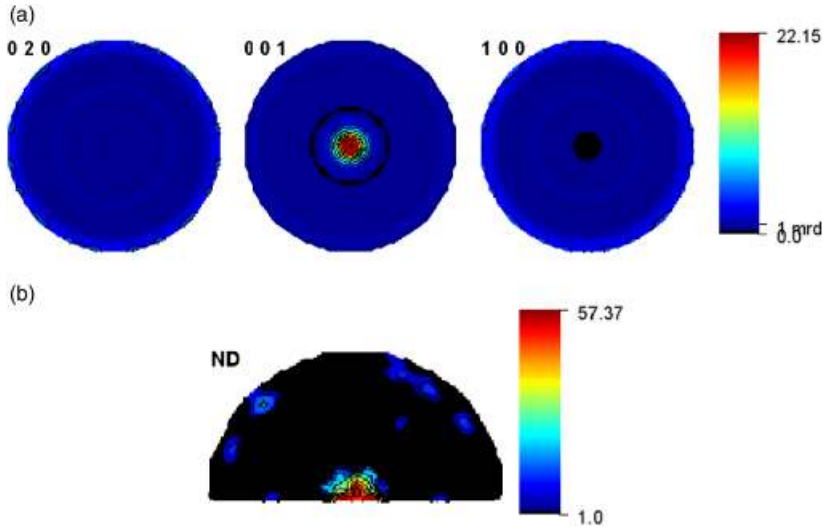

Fig. 4. (a) {020}, {001}, and {100} pole figures for the single-layer sample prepared at 30 MPa obtained after OD refinement (linear density scale, equal area projection) and (b) inverse pole figure calculated for the direction of the pressure (logarithmic density scale, equal area projection).

The reference sample elaborated at no imposed stress exhibits a maximum of the {001} poles of 3.48 mrd, more than six times less than for the single-layer sample prepared at 30 MPa. This shows that the texture strength increases with the pressing level and that the HP process is an efficient technique to obtain 349 textured ceramics. We also observe that the pole figures for this sample (Fig. 5b) indicate a minimum of 0.43, corresponding to 43% of the sample volume not aligned within the ⟨001⟩ fiber texture. The Rietveld refinement was obtained with larger reliability factors ($R_w = 6.81\%$, $R_{Bragg} = 5.32\%$, $R_{expected} = 5.89\%$) but with a GoF of only 1.33 and with no noticeable change of the cell parameters ($a = 4.8911(5)$ Å,

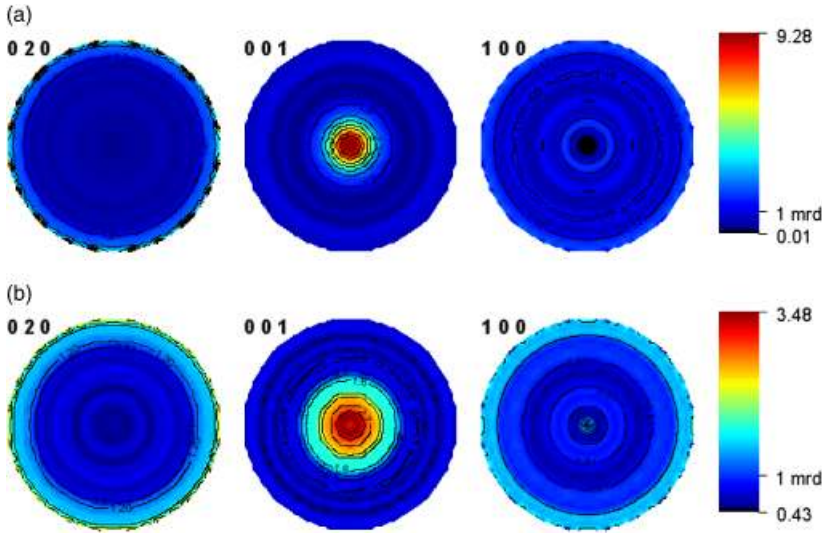

Fig. 5. {020}, {001}, and {100} pole figures for (a) the single-layer sample prepared at 13 MPa and (b) the reference sample processed without any applied stress, obtained after OD refinement (linear density scale, equal area projection).

$b = 36.339(5)$ Å, $c = 10.8227(2)$ Å, $\beta = 98.806(2)$) in comparison with the sample prepared at 30 MPa. The OD refinement exhibits lower reliability factors ($R_w = 3.11\%$ and $R_{Bragg} = 3.49\%$) correspondingly to a lower texture index $F^2 = 5$ mrd^2.[18] The relatively large Rietveld reliability factors are mainly due to the presence of still unidentified peaks. The maximum of the {001} poles, cell parameters, and reliability factors for the samples pressed at various pressing levels are summarized in Table I. A monotonous increase of the texture with σ is clearly seen from the {001} pole maxima, while cell parameters do not show significant evolution.

Mechanical and Thermal Properties

Instrumented nanoindentation technique was used to check the Young's modulus, E, and the hardness, H, in two directions: parallel (E^{ab} and H^{ab}) and perpendicular (E^{c} and H^{c}) to the HP axis. For each sample five areas were chosen for the nanoindentation tests. In each area, a batch of nine impressions, arranged in a 3×3 pattern, was performed. The pattern of residual impressions, left on an area of the HP sample prepared at 30 MPa after the Berkovich tip was withdrawn, is shown on the microphotograph of Fig. 6a. During the indentation test, the applied load P is continuously measured versus the indenter displacement, h. The load–displacement curve is obtained from a complete loading–unloading cycle (Fig. 6b). The derived hardness–displacement and Young's modulus–displacement curves are shown in Fig. 6c. For the determination of E^{c} and H^{c}, 10 impressions, arranged in a 2×5 array, were made on the mirror-polished cross section of the samples. The average values of Young's modulus, E^{ab} and E^{c}, and hardness, H^{ab} and H^{c}, are plotted versus the HP stress, σ, in Figs. 7a and b.

Mechanical properties are considerably improved with the HP stress σ. The in-plane Young's modulus, E^{ab}, and the strength, $\sigma_R{}^{ab}$, increase drastically from 10 ± 2 to 53 ± 8 GPa (Fig. 7a) and from 18 ± 0.2 to 198 ± 4 MPa, respectively, as the HP stress σ increases from 0 to 5 MPa. In this stress range, the bulk density of the 349 ceramics is greatly enhanced from 60% to 90.5% while the maximum of the {001} poles only increases from 3.48 to 7.82 mrd. This shows that the enhancement of E^{ab} is essentially related to the strong densification of the ceramics, and to a lesser extent to the texture strength. For σ values above 5 MPa, the increase of E^{ab} with σ is relatively weak although the texture strength increases significantly. This confirms the primacy of the influence of the bulk density on the Young's modulus values (Table I). E^{ab} reaches 56 ± 4 GPa for the single-layer sample highly densified under 30 MPa, that is five times larger compared with

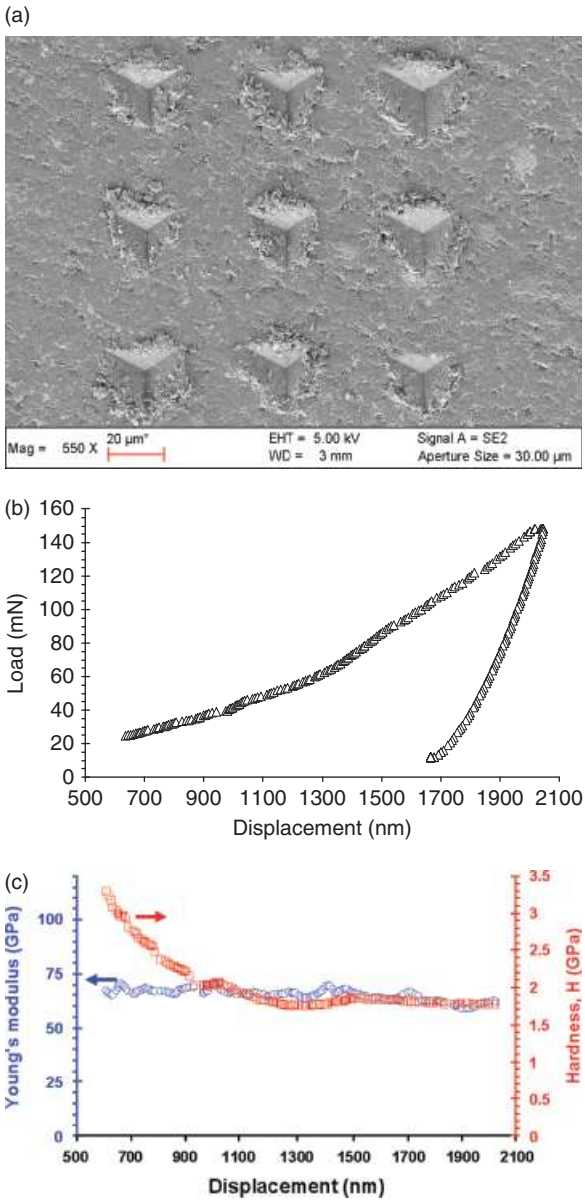

Fig. 6. (a) A 3 × 3 matrix pattern of residual impressions introduced on a zone of the single-layer sample; (b) load–displacement curve obtained from a complete loading–unloading cycle; and (c) derived hardness–displacement and Young's modulus–displacement curves.

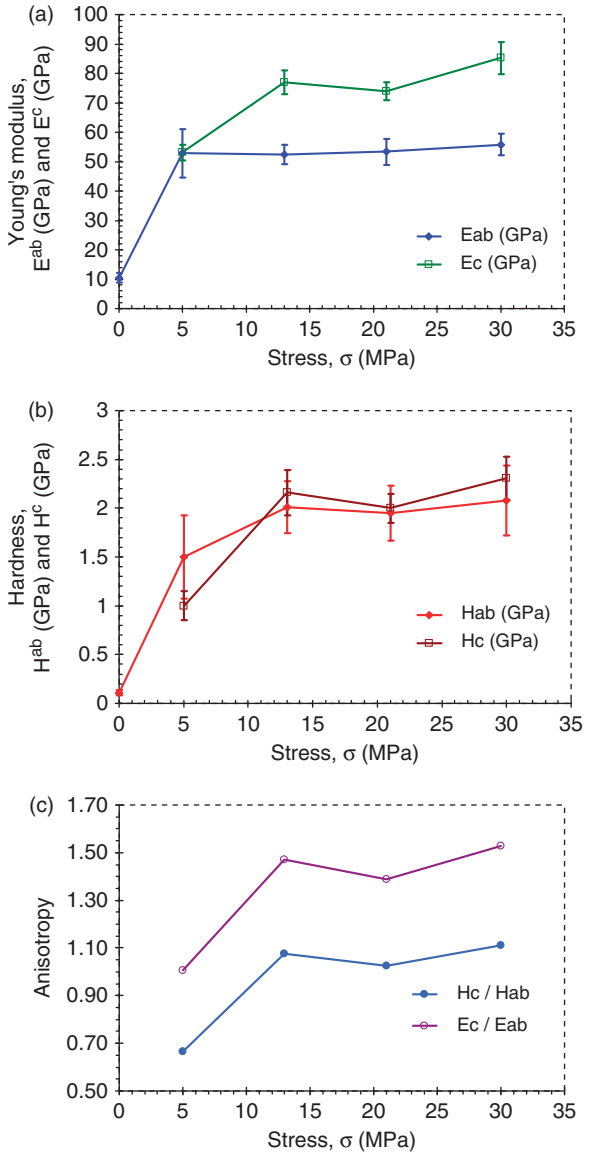

Fig. 7. (a) Young's modulus, E^{ab} and E^c; (b) hardness, H^{ab} and H^c; and (c) anisotropy factors $\frac{E^c}{E^{ab}}$ and $\frac{H^c}{H^{ab}}$ versus the hot-pressing stress σ.

the reference sample. ${\sigma_R}^{ab}$ displayed a value of 249 ± 4 MPa for the multilayer sample, corresponding to an improvement of almost 14 times. The increase of the out-of-plane Young's modulus E^c is much more important than the in-plane value (Fig. 7a) as σ is increased, and this is relevant to the bulk density reinforcement, particularly in the low σ range. However, at larger σ values, E^c displays a steeper increase than E^{ab}, which can be correlated to the texture strength increase. E^c reaches 85 ± 5 GPa for the single-layer sample hot-pressed under 30 MPa. The stiffness anisotropy, estimated by the $\frac{E^c}{E^{ab}}$ ratio (Fig. 7c), increases with σ up to 1.53 for this latter sample.

The hardness evolution shows a similar trend. H^{ab} and H^c remarkably increase with the HP stress level. H^{ab} increases drastically from 0.11 ± 0.03 GPa for the reference sample to 1.5 ± 0.4 GPa for the single-layer sample hot-pressed under 5 MPa, due to the same factors evoked for the Young's modulus. H^{ab} reaches 2.1 ± 0.4 GPa for the single-layer consolidated at 30 MPa, corresponding to a 19-time increase compared with the reference sample. H^c values tend to exceed H^{ab} for σ larger than 13 MPa, that is when the texture strength influence becomes more important (the maximum of the {001} poles are then >9 mrd). H^c is 2.3 ± 0.2 GPa for a pressing stress of 30 MPa, which is 21-fold the reference sample's value. The higher hardness anisotropy, $\frac{H^c}{H^{ab}} = 1.11$, is obtained for $\sigma = 30$ MPa (Fig. 7c).

The multilayer sample was found to exhibit similar values of the mechanical properties ($E^{ab} = 54 \pm 5$ GPa and $H^{ab} = 1.9 \pm 0.3$ GPa) as the ones of the single-layer sample processed at 30 MPa. This means that HP of stacked layers does not induce any noticeable perturbation of the microstructure and texture, in regard to the in-plane mechanical properties. However, for these thick samples $E^c = 71.5 \pm 2.5$ GPa and $H^c = 1.8 \pm 0.1$ GPa; these values are significantly lower than those obtained for the single-layer samples also pressed at 30 MPa. It can be concluded that many defects may remain at the interfaces between the stacked layers, despite the HP stress applied.

Figure 8 shows the thermal expansion behavior in the temperature range 50–900°C for the reference sample and multilayer sample; the latter was prepared by HP a stack of single layers previously textured at 30 MPa. The thermal expansion was measured parallel (*c*-axis) and perpendicular (in *ab* plane) to the pressing axis. It appears a clear difference in thermo-mechanical behavior for the both directions. The difference in the thermal behavior along the heating and the cooling paths may be explained by the effects of irreversible phenomena upon heating at the grain boundaries. While the coefficient of thermal expansion (CTE) of the reference sample is $\alpha_{ref} = 12.6 \times 10^{-6}$/K, those of the multilayer sample measured parallel and perpendicular to the stress direction are $\alpha_c = 15 \times 10^{-6}$/K and $\alpha_{ab} = 7.3 \times 10^{-6}$/K, respectively. The CTE ratio ($\frac{\alpha_c}{\alpha_{ab}} \approx 2$)

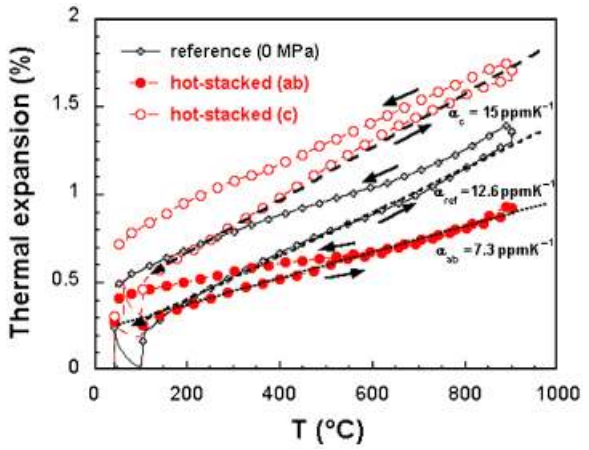

Fig. 8. Thermo-mechanical analysis of the reference sample processed without any applied stress and following the directions parallel (c) and perpendicular (ab) to the pressing axis for the multilayer sample (hot-stacked sample).

associated with the ranking order $\alpha_{ab} < \alpha_{ref} < \alpha_c$ shows the influence of the grain boundary density and thus the particular effect of the HP process. Moreover, the in-plane thermal expansion α_{ab} of 349 textured ceramics is close to some oxide materials (e.g., alumna: 8×10^{-6}/K), while α_c is similar to that of metals (e.g., copper: 16×10^{-6}/K). Consequently, the 349 textured ceramics can be connected to other materials for electrical contact (e.g., metal) or for thermal contact (e.g., Al_2O_3 plate) in TE modules, with a great reliability and improved efficiency.

Transport Properties

Figure 9a shows the temperature dependence of the electrical resistivity, ρ^{ab}, for the different HP stress levels, in the 5–350 K range. The current was injected perpendicular to the HP direction, that is the current flows in the mean *ab* planes, especially for the strongly textured HP samples (Table I). The $\rho^{ab}(T)$ curves show the same trend: the transition from metal to insulator occurs around 50 K. This is in agreement with earlier reports[2,23,24] on this type of TE oxide. ρ^{ab} is strongly reduced as the HP stress level is increased up to 13 MPa. This reduction correlates with a higher connection between the grains (Fig. 2a and b) and a stronger texture. The room-temperature resistivity, $\rho_{300\,K}{}^{ab}$, of the single-layer sample hot-pressed at 30 MPa is 6.1 mΩ.cm, which is almost seven times smaller than that of the

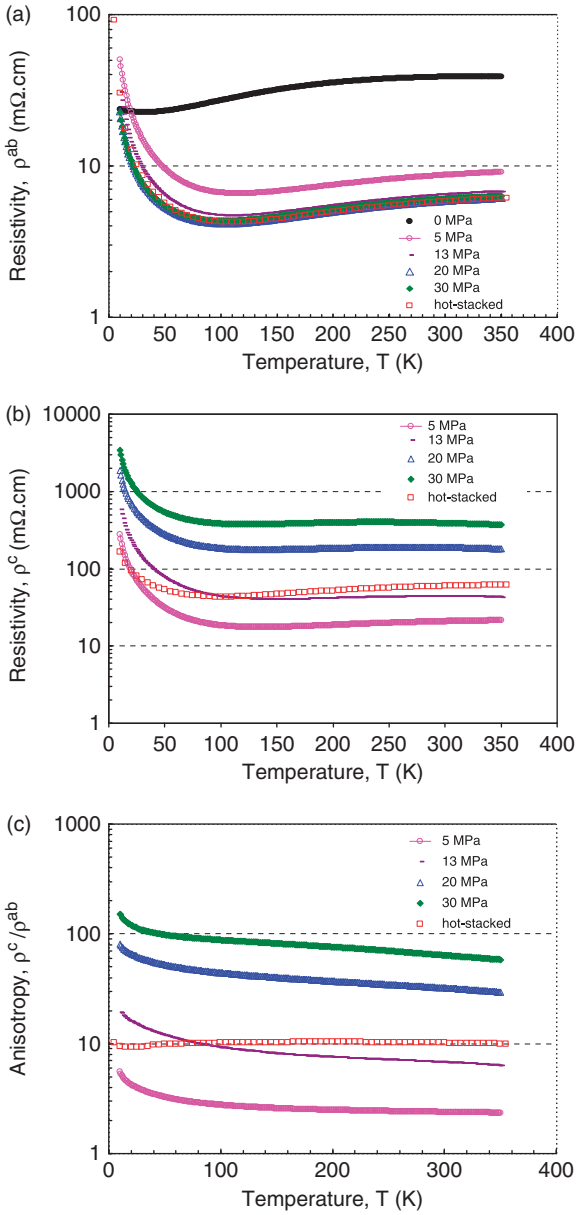

Fig. 9. Temperature dependence of electrical resistivity measured at low-temperature range for 349 ceramics: (a) perpendicular, ρ^{ab}, and (b) parallel, ρ^{c}, to the hot-pressing axis. (c) Temperature dependence of the resistivity anisotropy, $\frac{\rho^c}{\rho^{ab}}$.

reference sample. This value is among the best published in the literature.[7,10,25] An interesting result is that the multilayer sample displays the same ρ^{ab} values as the single-layer sample prepared at 30 MPa, which supports the mechanical property results, that is the HP of

stacked layers does not perturb the in-plane microstructure and texture strength of individual layers. The $\rho^c(T)$ curves obtained in the same temperature range are shown in Fig. 9b. The current was injected parallel to the HP direction. These curves display the same temperature dependence as the $\rho^{ab}(T)$ ones, but the resistivity values increase drastically as the HP stress level is increased. This increase in ρ^c values is mainly related to higher out-plane grain boundary density and texture strength. The $\rho^c{}_{300\,K}$ of the single-layer sample processed at 30 MPa reaches 390 mΩ.cm.

The multilayer sample exhibits ρ^c values much smaller than those of the single-layer sample processed at 30 MPa. An explanation of this lower ρ^c values could be due to the second HP cycle applied as soldering stage for stacking the different single layers. This second thermo-mechanical stacking probably induced more *ab* planes favorable to carry the current into the bulk sample.

The anisotropy of the resistivity for these materials is evidenced in Fig. 9c, where the factor $\frac{\rho^c}{\rho^{ab}}$ is plotted versus temperature. $\frac{\rho^c}{\rho^{ab}}$ increases greatly with the HP stress level and reaches 64 at 300 K for the single-layer sample processed at 30 MPa. This value is much larger than those reported for 349 single crystals,[2] which can be explained by the following reasons: (i) the in-plane resistivity, ρ^{ab}, obtained at 300 K for our 349 textured polycrystalline ceramics (6.1 mΩ.cm) is lower than the values reported for 349 single crystals by Masset *et al.*,[2] (12 mΩ.cm), and Bhattacharya *et al.* ($\sim$19 mΩ.cm).[26] Our result is in accordance with numerous publications in which comparable values are reported on ρ^{ab} measurements at 300 K on 349 polycrystalline materials. They also show lower values than those obtained on 349 single crystals. We can quote, for example, Zhou *et al.*[7] who reported 11.4 and 6.1 mΩ.cm for 349 polycrystalline ceramics processed by SPS process and by combination of the MA technique and SPS treatment,[7] respectively. Xu *et al.*[5] also reported an electrical conductivity of 95 S/cm at 300 K, corresponding to $\rho^{ab} = 10.5$ mΩ.cm, for 349 polycrystalline ceramics processed by HP. (ii) The out-plane resistivity, $\rho_{300\,K}{}^c$, measured on our 349 textured ceramics (390 mΩcm) is much higher than those reported for single crystals. For example, reported values are 200 mΩ.cm [2] and $\sim$92.5 mΩ.cm.[26] The particularly high values found on our bulk materials can be explained by the higher out-plane grain boundary density due to the remarkable decrease of the thickness upon HP at 30 MPa (Table I), and to the strong alignment of the platelets in the *ab* planes, that is the strong texture resulting from the HP process.

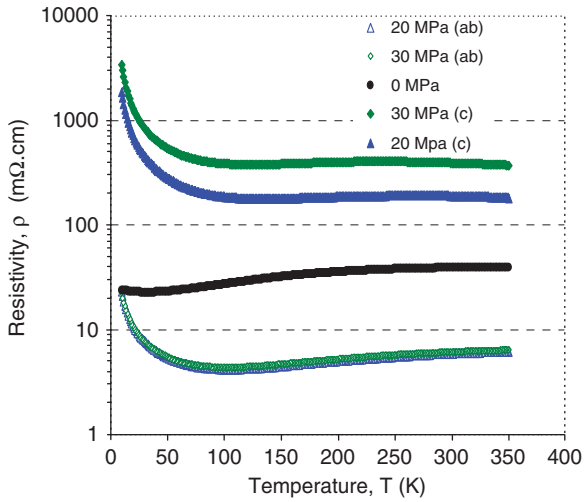

Fig. 10. Temperature dependence of electrical resistivity for the reference sample lies between the resistivity values, ρ^{ab} and ρ^c, of the HP samples processed at high stress (20 and 30 MPa).

Consequently, the anisotropy ratio is larger in the 349 bulk ceramics than in the single crystals.

Our $\frac{\rho^c}{\rho^{ab}}$ value obtained at 300 K is also higher than that reported for 349 bulk ceramics processed by SPS process[10] because of the stronger texture.

The multilayer sample displays a merely constant resistivity anisotropy factor $\frac{\rho^c}{\rho^{ab}} \approx 10$, which is much smaller compared with the values recorded for the single-layer samples hot-pressed at 30 MPa.

It should be noticed that, at temperature above 150 K, the resistivity of the weakly textured sample, processed without any applied stress, lies between the resistivity values measured perpendicular, ρ^{ab}, and parallel, ρ^c, to the HP axis of the HP samples, and in particular the ones exhibiting high anisotropy resistivity values processed at 20 and 30 MPa. The reference sample resistivity is closer to the resistivity values, ρ^{ab}, and to the values of the HP sample processed at 20 MPa than to those of the one elaborated at 30 MPa (Fig. 10), which is in agreement with the statistical quite random distribution of the crystallites in the former.

In the high-temperature range from 350 to 900 K, ρ^{ab} also decreases as σ is increased (Fig. 11a) because of the same factors evoked for reducing ρ^{ab} values in low-temperature range. At 900 K the ρ^{ab} is 5.25 mΩ.cm, which is one of the lowest values reported so far. Figure

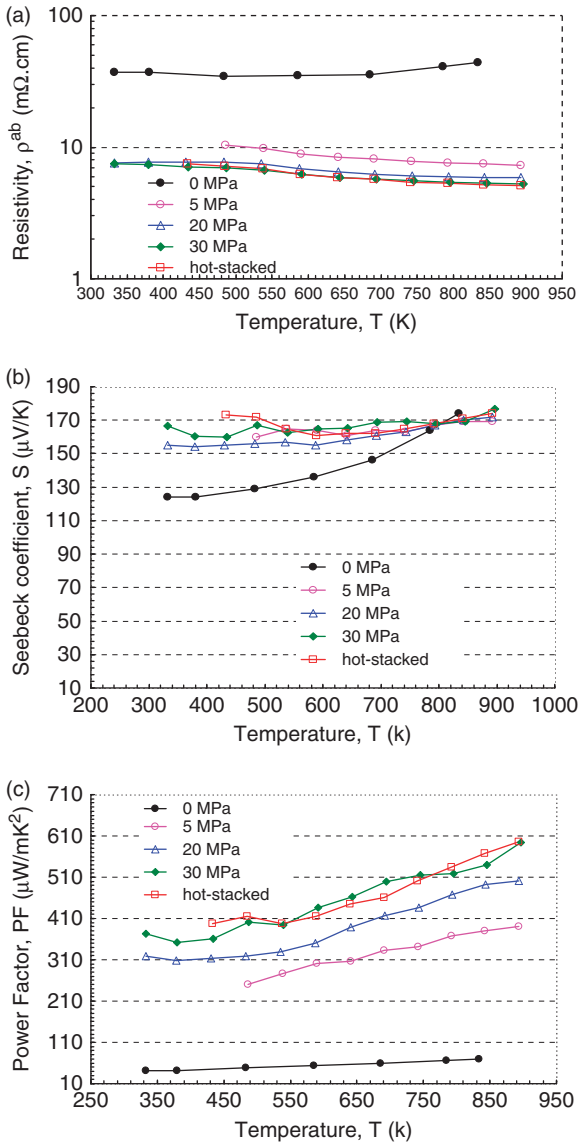

Fig. 11. Temperature dependence of (a) electrical resistivity, ρ^{ab}, and (b) Seebeck coefficient, S^{ab}, measured at high-temperature range for 349 samples processed under various stress levels and multilayer samples. (c) Temperature dependence of the power factor $PF^{ab} = \frac{S^{ab2}}{\rho^{ab}}$.

11b shows the temperature dependence of the Seebeck coefficient, S^{ab}, also measured in the direction perpendicular to the HP axis. The S^{ab} values are nearly independent of HP stress, but they increase with temperature up to 177 μV/K at 900 K for the HP sample at 30 MPa. The positive value indicates that the majority of charge carriers is hole like and the values observed on our 349 ceramics are consistent with data published in the literature.[7,10,25] Because ρ^{ab} is decreased without lowering S^{ab}, the power factor, $PF^{ab} = \frac{S^{ab2}}{\rho^{ab}}$, improves with σ and reaches 595 μW/m/K^2 at 900 K for the single-layer sample processed at 30 MPa (Fig. 11c). This PF^{ab} value is higher than that reported for 349 ceramics processed by SPS process,[7] by combination of the MA technique and SPS treatment[7] and by HP.[25] The multilayer sample displays the same PF values as the single-layer sample elaborated at 30 MPa.

Conclusion

Textured 349 ceramics were elaborated using the HP process. The mechanical properties were shown to improve well with the applied stress, σ, and anisotropy of the elastic modulus, $\frac{E^c}{E^{ab}}$, and of the hardness, $\frac{H^c}{H^{ab}}$, occur. The anisotropy ratios are 1.53 and 1.11, respectively, for the sample prepared at 30 MPa. The resistivity anisotropy increases drastically with σ and reaches 64 at 300 K for a processing stress of 30 MPa. The power factor perpendicularly to the stress direction is greatly improved with σ and reaches 595 μW/m/K^2 at 900 K. The multilayer sample was successfully prepared and showed to keep the same performances than the 30 MPa HP single-layer samples. This thick sample will be used to design and perform TE modules. We are processing much thicker multilayer samples in order to measure the Seebeck coefficient parallel to the pressing axis, S^c, the thermal conductivity in two directions (κ^{ab} and κ^c), and to check the toughness parameter for our 349 ceramics.

Acknowledgments

D. Kenfaui and the authors acknowledge the Conseil Régional de Basse Normandie, France for its fellowship financial and financial participation for experimental setup used in this work, respectively.

References

1. S. Li, R. Funahashi, I. Matsubara, K. Ueno, and H. Yamada, "High Temperature Thermoelectric Properties of Oxide $Ca_9Co_{12}O_{28}$," *J. Mater. Chem.*, 9 1659–1660 (1999).
2. A. C. Masset, *et al.*, "Misfit-Layered Cobaltite with an Anisotropic Giant Magnetoresistance: $Ca_3Co_4O_9$," *Phys. Rev. B*, 62 166–175 (2000).

3. M. Shikano and R. Funahashi, "Electrical and Thermal Properties of Single-Crystalline $(Ca_2CoO_3)_{0.7} \cdot CoO_2$ with a $Ca_3Co_4O_9$ Structure," *Appl. Phys. Lett.*, 82 1851–1853 (2003).
4. M. Hervieu, Ph. Boullay, C. Michel, A. Maignan, and B. Raveau, "A New Family of Misfit Layered Oxides with Double Rock Salt Layers $Bi_x(A_{0.75\pm\varepsilon}Bi_{0.256\pm\varepsilon}O)_{(3+3x)/2}MO_2$ (A = Ca, Sr and M = Co, Cr)," *J. Solid State Chem.*, 142 305–318 (1999).
5. G. Xu, R. Funahashi, M. Shikano, I. Matsubara, and Y. Zhou, "Thermoelectric Properties of the Bi- and Na-Substituted $Ca_3Co_4O_9$ System," *J. Appl. Phys. Lett.*, 80 3760–3762 (2002).
6. R. Funahashi, I. Matsubara, and S. Sodeoka, "Thermoelectric Properties of $Bi_2Sr_2Co_2O_x$ Polycrystalline Material," *Appl. Phys. Lett.*, 76 2385–2387 (2000).
7. Y. Zhou, *et al.*, "Thermoelectric Properties of Highly Grain-Aligned and Densified Co-Based Oxide Ceramics," *J. Appl. Phys.*, 93 2653–2658 (2003).
8. A. Maignan, S Hebert, D. Pelloquin, C. Michel, and J. Hejtmanek, "Thermoelectric Power Enhancement in Misfit Cobaltites," *J. Appl. Phys.*, 92 1964–1967 (2000).
9. M. Prevel, *et al.*, "Textured $Ca_3Co_4O_9$ Thermoelectric Oxides by Thermoforging Process," *J. Appl. Phys.*, 98 93706–93709 (2005).
10. Y. Zhang, J. Zhang, and Q. Lu, "Synthesis of Highly Textured $Ca_3Co_4O_9$ Ceramics by Spark Plasma Sintering," *Ceram. Int.*, 33 1305–1308 (2007).
11. E. Woermann and A. Muan, "Phase Equilibria in the System CaO–Cobalt Oxide in Air," *J. Inorg. Nucl. Chem.*, 32 1455–1459 (1970).
12. V. Rouessac, J. Wang, J. Provost, and G. Desgardin, "Processing and Superconducting Properties of Highly Textured Bi(Pb)-2223 Ceramics by Sinter-Forging," *Phys. C*, 268 225–232 (1996).
13. J. Ricote and D. Chateigner, "Quantitative Texture Analysis Applied to the Study of Preferential Orientations in Ferroelectric Thin Films," *Bol. Soc. Esp. Ceram. Vidrio*, 38 [6] 587–591 (1999).
14. D. Chateigner, ed. *Combined Analysis: Structure–Texture–Microstructure–Phase–Stresses–Reflectivity Analysis by X-Ray and Neutron Scattering*, ISTE, London, 2004, p. 147. Available at http://www.ecole.ensicaen.fr/~chateign/texture/combined.pdf (accessed July 21, 2009).
15. L. Lutterotti, S. Matthies, and H.-R. Wenk, "MAUD (Material Analysis Using Diffraction): A User Friendly Java Program for Rietveld Texture Analysis and More," *Textures of Materials: Proceedings of ICOTOM14*, ed., J. A. Spunar. National Research Council of Canada, Ottawa, 1599–1604, 1999.
16. S. Matthies, G. Vinel, and K. Helming, *Standard Distributions in Texture Analysis*, Vol. 1. eds., S. Matthies, G. Vinel, and K. Helming. Akademie-Verlag, Berlin, 1–449, 1987.
17. L. Lutterotti, D. Chateigner, S. Ferrari, and J. Ricote, "Texture, Residual Stress and Structural Analysis of Thin Films Using a Combined X-ray Analysis," *Thin Solid Films*, 450 34–41 (2004).
18. D. Chateigner, "Reliability Criteria in Quantitative Texture Analysis with Experimental and Simulated Orientation Distributions," *J. Appl. Crystallogr.*, 38 603–611 (2005).
19. E. Guilmeau, D. Chateigner, J. Noudem, R. Funahashi, S. Horii, and B. Ouladdiaf, "Rietveld Texture Analysis of Complex Oxides: Examples of polyphased Bi2223 superconducting and Co349 Thermoelectric Textured Ceramics Characterization Using Neutron and X-Ray Diffraction," *J. Appl. Crystallogr.*, 38 199–210 (2005).
20. W. C. Oliver and G. M. Pharr, "An Improved Technique for Determining Hardness and Elastic Modulus Using Load and Sensing Indentation Experiments," *J. Mater. Res.*, 7 1564–1583 (1992).
21. J. Woirgard and J. C. Daegenton, "An Alternative Method for Penetration Depth Determination in Nanoindentation Measurement," *J. Mater. Res.*, 12 [9] 2455–2458 (1997).
22. H. C. Montgomery, "Method for Measuring Electrical Resistivity of Anisotropic Materials," *J. Appl. Phys.*, 42 2971–2975 (1971).
23. T. Fujii, I. Terasaki, T. Watanabe, and A. Matsuda, "Large In-Plane Anisotropy on Resistivity and Thermopower in the Misfit Layered Oxide $Bi_{2-x}Pb_xSr_2Co_2O_y$," *Jpn. J. Appl. Phys.*, 41 783–786 (2002).
24. T. Yamamoto, *et al.*, "Structural Phase Transition and Metallic Behavior in Misfit Layered (Bi,Pb)–Sr–Co–O System," *Jpn. J. Appl. Phys.*, 39 747–750 (2000).
25. M. Mikami, E. Guilmeau, R. Funahashi, K. Chong, and D. Chateigner, "Enhancement of Electrical Properties of the Thermoelectric Compound $Ca_3Co_4O_9$ Through Use of Large-Grained Powder," *J. Mater. Res.*, 20 [9] 2491–2497 (2005).
26. S. Bhattacharya, *et al.*, "Anisotropy Electrical Transport Studies of $Ca_3Co_4O_9$ Single Crystals Grown by the Flux Method," *J. Cryst. Growth*, 277 246–251 (2005).